Estimation of the Uncertainty in Daytime Cirrus Cloud Radiative Forcing and Heating Rates Due to Ice Crystal Optics

Erica K. Dolinar[1], James R. Campbell[1], Jared W. Marquis[2], Jasper R. Lewis[3], Simone Lolli[4], Ping Yang[5], Ellsworth J. Welton[6]

1. U.S. Naval Research Laboratory, Monterey, CA
2. University of North Dakota, Department of Atmospheric Sciences, Grand Forks, ND
3. Joint Center for Earth Systems Technology, University of Maryland, Baltimore County, Baltimore, Maryland
4. Consiglio Nazionale delle Ricerche, Istituto di Metodologie per l'Analisi Ambientale, Tito Scalo, Italy
5. Texas A&M University, Department of Atmospheric Sciences, College Station, Texas
6. NASA Goddard Space Flight Center, Greenbelt, MD

Corresponding author address: Erica K. Dolinar; 7 Grace Hopper Ave., Stop 2, Monterey, CA 93943
E-mail: erica.k.dolinar.civ@us.navy.mil

Abstract

The uncertainties in absolute daytime top-of-the-atmosphere (TOA) net cirrus cloud radiative forcing (CRF) and radiative heating rates are estimated at five Micro-Pulse Lidar Network (MPLNET) sites spanning the tropics to high-latitudes. One year of semi-transparent cirrus cloud (optical depth < 3.0 and cloud top temperature < –37 °C) measurements are subject to spectrally-consistent optical properties for nine different ice crystal habits, thus providing a range of possible forcing values. The annual average absolute daytime TOA net CRF is positive at Barbados, Kanpur, and, Singapore (0.59–0.67, 0.61–0.65, and 1.94–2.09 $W \cdot m^{-2}$, respectively), negative at Fairbanks (–0.67 to –0.28 $W \cdot m^{-2}$), and can regularly become positive or negative at Goddard Space Flight Center (GSFC) (–0.06 to 0.32 $W \cdot m^{-2}$). The TOA CRF depends on ice crystal shape; in particular, plates lead to relatively large absolute values that decreases for bullet rosettes and columns. Uncertainties in daytime cirrus cloud radiative properties are estimated as the standard deviation of all possible outcomes when considering the different particle habits individually. Annually, the average uncertainty of the absolute daytime TOA net CRF ranges from 0.50–1.80 $W \cdot m^{-2}$. In-cloud daytime net radiative heating rates are positive, on average, at all five sites (0.25–3.84 K/day) and have an estimated uncertainty of less than 0.30 K/day. The uncertainties in cirrus radiative forcing and heating that are characterized by assumptions regarding the ice crystal optical properties must be considered in downstream applications, including satellite retrievals and numerical weather prediction.

Significance Statement

Cirrus clouds are the single most common cloud type in Earth's atmosphere and, since they exist at high altitudes, are comprised of nonspherical ice crystals. Determining the impact of cirrus clouds on the global energy budget is therefore critical for climate studies and weather prediction. This is a difficult task, as ice crystals uniquely scatter and absorb radiant energy according to their size and shape. Here, the uncertainty in daytime semi-transparent cirrus cloud radiative properties is estimated, driven by assumptions related to ice crystal shape, at five locations around the globe using lidar measurements. The cirrus cloud radiative impact has a

systematic dependency on ice crystal shape, where plates lead to a relatively stronger greenhouse effect and columns lead to a stronger albedo effect.

I. Introduction

Clouds are among the most significant sources contributing to the scattering and absorption of radiant energy in the atmosphere (Liou and Yang 2016). Observing and modeling the interaction between clouds and radiation has long been a focus for assessing changes in Earth's climate (e.g., Ramanathan et al. 1989; Weilicki et al. 1995; Stevens and Schwartz 2012; Voigt et al. 2021). Still, clouds continue to be recognized as one of the largest sources of uncertainty in many modeling communities (Bonan et al. 2018; Zelinka et al. 2020; Jahangir et al. 2021). Ice-phase clouds are unique when compared against liquid-phase clouds due to their relatively higher altitudes, optical semi-transparency, and ability to preferentially scatter sunlight depending on the size and shape of ice crystals.

Ice crystals nucleate, grow, and aggregate primarily according to the ambient air temperature and supersaturation (Pruppacher and Klett 1997; Bailey and Hallett 2009), resulting in a number of preferential shapes (i.e., habit types). Radiative transfer modeling of ice crystals, for applications such as the development of satellite retrievals (Loeb et al., 2018), numerical weather prediction (Muskatel et al. 2021), and climate studies (Baran 2009; Liou and Yang 2016; Yang et al. 2018), requires an estimate of their single-scattering properties. In order to minimize the uncertainties associated with ice-phase cloud radiative transfer, much effort has been focused on resolving ice cloud optical properties from remote sensing measurements and retrievals (van Diedenhoven et al. 2012; 2013; 2020), in-situ cloud measurements (Baumgardner et al. 2017; Jarvinen and Schnaiter 2018; Xu et al. 2022), laboratory measurements (Järvinen et al. 2014), and numerical methods (Waterman 1971; Macke et al. 1995; Havemann and Baran 2001; Yang et al. 2013; Bi and Yang 2014; 2017; Stegmann et al. 2016).

Cirrus are particularly interesting because they are the most common individual cloud type in Earth's atmosphere, with an instantaneous global cloud fraction estimated at around 40% (Stubenrauch et al. 2013). Cirrus clouds are unique because, unlike all other clouds that only produce net negative effects on the global top-of-the-atmosphere (TOA) radiation budget during

daylight hours, cirrus clouds can produce either a net positive or net negative radiative effect (Stackhouse and Stephens 1991). Conversely, all clouds are net radiative warmers during nighttime. Cloud microphysical, geometric, and optical properties, in addition to surface properties, background meteorology, and solar geometry, all affect the sign and magnitude of the daytime TOA cloud radiative forcing (CRF). Accurately resolving the cirrus CRF is thus an important contextual baseline for climate studies and understanding the uncertainty is a necessary component. The *total* net TOA CRF is an aggregation of the daytime and nighttime components. Thus, correctly isolating changes in the sign of both daytime and nighttime terms, whether on the regional or global scale, is key for reconciling their overall role in climate. Understanding the changes in sign also helps to identify important trends in cloud–radiative processes that are driven by climate change.

Vertical radiative heating induced by clouds is another important climate feature that impacts the balance of energy within the atmospheric column. For example, cloud radiative heating has downstream implications on cloud lifecycle (Wall et al. 2020) and large-scale circulation patterns (e.g., Crueger and Stevens 2015; Harrop and Hartmann 2016). In fact, Lin et al. (2004) describe the importance of resolving vertical radiative heating within the atmosphere and theorize how errors in the predicted differential heating impact the magnitude and propagation of the Madden-Julian oscillation. Dolinar et al. (2019) provide an overview of the global average radiative heating caused by ice clouds, indicating that ice clouds are most efficient at radiatively warming the troposphere in the tropics and mid-latitudes where cloud heights are maximized but transition to net radiative coolers at higher latitudes.

This study utilizes ground-based lidar measurements as the basis for a series of radiative transfer simulation experiments aimed at constraining estimates of the daytime cirrus CRF, radiative heating rate profiles, and their systematic variance as a function of underlying optics assumptions. By applying a variety of ice cloud optical models to a singular dataset, we seek to properly attribute the relative uncertainty in daytime cirrus cloud radiative properties driven by paramterized single-scattering properties, with the goal of better informing the community of the signicance and presently open-ended nature of this fundamental element.

II. Data and Methods

a. Micropulse Lidar Network (MPLNET)

The NASA Micro-Pulse Lidar (MPL) Network (MPLNET) is a federated network of ground-based backscatter lidars that was initiated more than 20 years ago (Welton et al. 2001; 2018). Current information on the MPLNET project is available online (https://mplnet.gsfc.nasa.gov), including descriptions of MPLNET sites, data products, and public access to the data utilized here. For this study, MPLNET Version 3, Level 1 Normalized Relative Backscatter (NRB) signal products and Version 3, Level 1 Cloud products were used. However, quality flags from the NRB product were used to remove cloud retrievals from potentially poor quality signals. The NRB products contain the energy normalized, range corrected lidar signals at 1 minute temporal and 75 meter vertical resolution, for 24 hour continuous observations. The cloud products contain cloud base and top heights, cloud phase, and estimates of cirrus cloud optical depth (COD) and extinction profiles (Lewis et al. 2016).

Single-layer (i.e., no aerosol, other cloud, or precipitation) cirrus clouds are sub-sampled from unconstrained MPLNET retrievals (Campbell et al. 2008; 2015; Lewis et al. 2016) using bookend lidar ratios of 20 and 30 sr to estimate the upper and lower bounds of the daytime cirrus CRF (Yorks et al. 2011). The cloud extinction coefficient profile is then derived using these lidar ratios. Cirrus are subset from other clouds by restricting COD to 0.005–3.0, cloud-top (-base) temperature less than –37 °C (–25 °C) (Campbell et al. 2016). Meteorological profiles of temperature, specific humidity, and ozone, which are needed for radiative transfer, come from Goddard Earth Observing System Model version 5 (GEOS-5) atmospheric general circulation model (Rienecker et al. 2008; Molod et al. 2012).

Campbell et al. (2016), Lolli et al. (2017), and Campbell et al. (2021) analyzed the daytime cirrus CRF from multiple years of MPLNET datasets. These prior studies focused on establishing foundational knowledge about cirrus radiative properties measured by ground-based lidars, including the gradient in the total (daytime + nighttime) and daytime-only TOA net CRF terms. Here, we extend upon this trilogy of papers by applying their methods to emphasize how assumptions made about ice crystal scattering and absorption influence cirrus radiative

properties at five sites spanning the northern hemisphere tropics to high-latitudes. Measurements from one year at Singapore (2010; 1.298 °N; 103.780 °E), Barbados (2013; 13.170 °N; 59.430 °W), Kanpur, India (2012; 26.519 °N; 80.233 °E), Goddard Space Flight Center (GSFC), Greenbelt, MD, USA (2012; 39.993 °N; 76.840 °W), and Fairbanks, AK, USA (2017; 64.859 °N; –147.849 °W) are analyzed. In total, GSFC (Kanpur) has the largest (smallest) relative record of daytime optically thin cirrus; annual totals and the monthly variation in daytime profile counts at each site are provided in Fig. 1a.

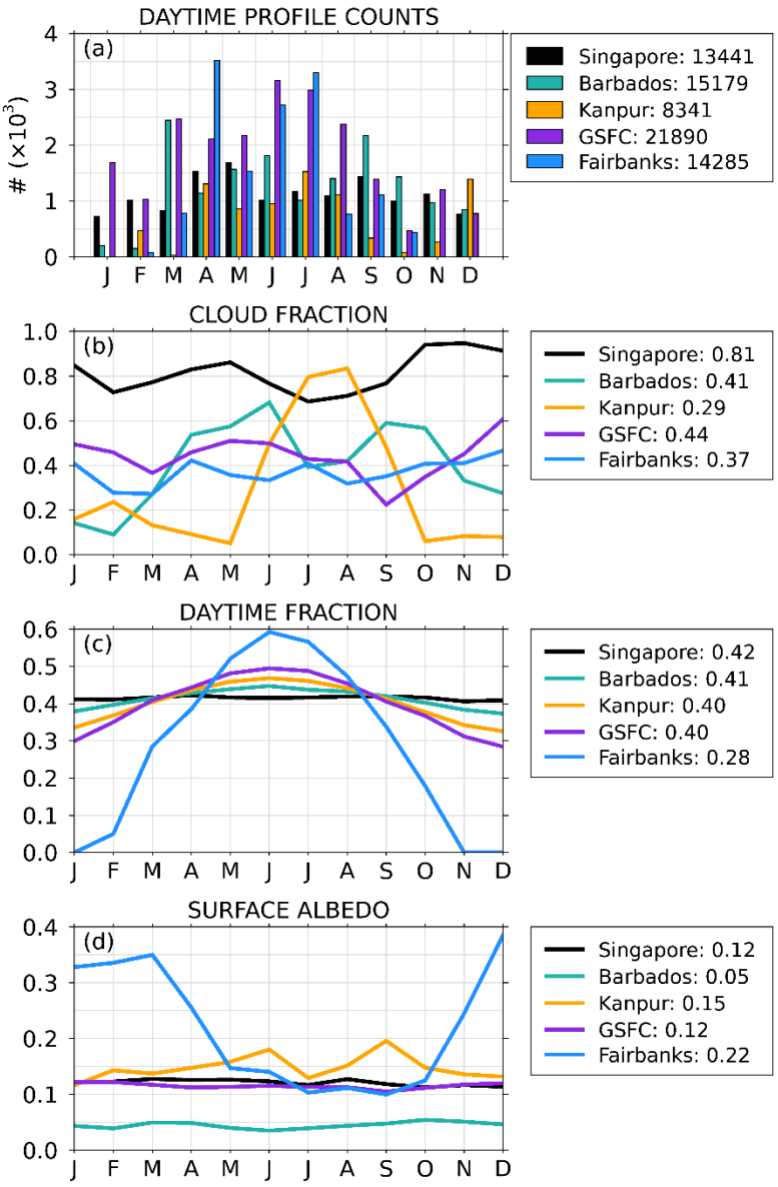


Figure 1: Monthly (a) total daytime cirrus cloud profile counts, (b) mean optically thin cirrus cloud fractions (CF) based on CALIOP measurements, (c) mean daytime fractions (DF), and (d) mean surface albedos from

CERES measurements for each MPLNET site; Singapore (black), Barbados (green), Kanpur (yellow), GSFC (purple), Fairbanks (blue). Annual totals and averages are provided in the legends.

b. Ice cloud optical properties

Yang et al. (2019) provide a comprehensive review of the latest computational capabilities for solving the optical properties of ice crystals. Aircraft measurements show that ice clouds are comprised of ice crystals of varying shapes, or a mixture of shapes, and sizes that cluster according to different environmental parameters, such as temperature and supersaturation (Pruppacher and Klett 1997). As such, there is a compulsory need for representing ice particle optical properties in a suitably robust manner capable of use over an extensive possibility of conditions. The benefit of optical models bound by numerical methods is the ability to represent the scattering and absorption properties of ice crystals across a wide range of wavelengths and particle sizes. In-situ measurements are limited to sampled portions of the cloud and laboratory measurements are taken in highly controlled environments. It is presently unclear whether these methods meet the threshold for capably representing the full array of possible ice physical properties (e.g., Dolinar et al. 2022). Synthetic optical models also have their limitations, as described in Yang et al. (2013). However, they represent a spectrally-consistent depiction of ice crystal optics across a wide range of ice crystal sizes.

Yang et al. (2013) and Bi and Yang (2014; 2017) document a library of optical scattering, absorption, and polarization properties at wavelengths from 0.2–100 μm for nine ice crystal habits (with maximum diameters from 2–10,000 μm): plates, 5-element plate aggregates, 10-element plate aggregates, droxtal, hollow bullet rosettes, solid bullet rosettes, hollow columns, hexagonal columns, and 8-element column aggregates. Particle surface roughness is also taken into account for each shape, with three distinct values for the degree of particle surface roughness: smooth, moderately roughened, and severely roughened. In this study, the single-scattering properties of all nine ice crystal habits are matched to the bands of a common community-recognized radiative transfer model.

The optical properties driving ice cloud radiative transfer are the vertically-resolved spectral single-scattering albedo, asymmetry factor, and optical depth. Figure 2 shows the single-scattering albedos and asymmetry factors for each of the nine ice crystal habits at two

wavelengths. Single-scattering albedo refers to the ratio of scattering efficiency to total extinction efficiency, where a value of one (zero) indicates all particle extinction is caused by scattering (absorption). The single-scattering albedo at 2.2 µm is, on average, larger than at 21.5 µm by 0.168, indicating a higher scattering (absorption) efficiency at solar (infrared) wavelengths; however, the spread among the nine habits is larger at 21.5 µm. At both wavelengths, bullet rosettes consistently have a higher single-scattering albedo compared with the other habits (except for plates in the infrared), meaning they are more efficient scatterers. The spread in single-scattering albedo is smaller at solar wavelengths but remains less than 5% over all wavelengths (not shown).

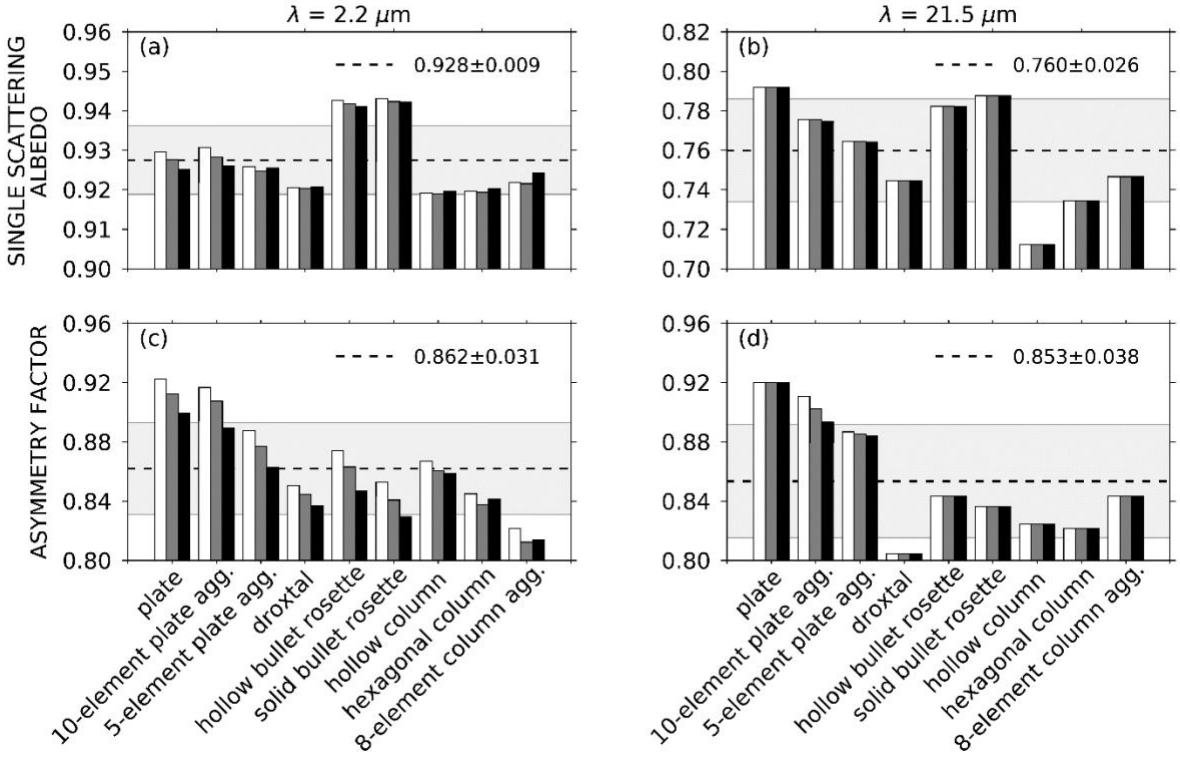


Figure 2: (a–b) Single scattering albedo and (c–d) asymmetry factor for each of the nine ice crystal habits with three levels of roughness; smooth (white), moderate (grey), and severe (black). Values are provided at Fu-Liou-Gu bands 4 and 16 (2.2 and 21.5 µm, respectively) for an effective diameter of 40 µm. The average and standard deviation are provided for each.

Asymmetry factor describes the overall asymmetry of the angular distribution of radiation scattered by a particle: larger asymmetry factors lead to stronger scattering in the forward hemisphere of angular space around an ice crystal. At both wavelengths, the asymmetry factor is largest for plates and decreases for bullet rosettes and columns. While the average and

standard deviation in asymmetry factor between the two wavelengths is within about 1%, there is stronger dependence to roughness at the solar wavelength and for plates/bullet rosettes. Yang et al. (2013) reports that the method for assuming severe roughening of ice crystals leads to a decrease in the asymmetry factor at solar wavelengths, which evidently provides better consistency of ice cloud optical thickness at both solar and infrared wavelengths.

By assuming every one of these ice crystal habit models in our radiative transfer code, we can solve a range of possible cirrus cloud radiative properties, thereby estimating the uncertainty. When computing this uncertainty, both the average and standard deviation in cloud radiative properties are solved across all optical models. Standard deviation defines the absolute uncertainty.

c. Fu-Liou-Gu radiative transfer model

The Fu-Liou-Gu (FLG) one-dimensional radiative transfer model (Fu and Liou 1992; 1993; Gu et al. 2003; 2011) computes the instantaneous shortwave (SW; six bands from 0.2–4.0 μm) and longwave (LW; twelve bands from 4.5–1000 μm) fluxes needed for analyzing the TOA CRF and heating rates. FLG has been modified to account for recent upgrades to the methods by which ice clouds are physically and optically characterized in the model. For example, Fu and Liou (1993) solved and spectrally spread the optical depth of ice clouds based on the cloud ice water content and effective particle diameter (D_e). Note that the D_e used in the present study is specified as $D_e=1.5V/A_p$, where V and A_p are the total volume and projected area of an ice crystal ensemble of interest, respectively, and is different from Fu and Liou (1993). The 532 nm lidar-derived extinction coefficient is converted to a vertically resolved optical depth and extended to the other FLG bands based on a wavelength-dependent extinction efficiency term. Still, the ice cloud D_e is required for estimating single scattering albedo and asymmetry factor. In this study, cirrus D_e is solved at the 75 m vertical lidar range bins according to Dolinar et al. (2022) (hereafter D22), and is a function of latitude, temperature, and lidar extinction. Calculation of bulk optical properties is performed by applying a gamma ice-crystal size distribution following Marquis et al. (2023).

III. Results

a. Cirrus cloud properties

One year of single-layer cirrus cloud profiles from five MPLNET sites are processed for this study. Only daytime cloud profiles are analyzed for the purpose of depicting the dual positive/negative nature of the TOA net CRF across the sites. Daytime is defined by Campbell et al. (2016) as periods when the incoming TOA SW flux exceeds that of the combined outgoing SW and LW flux at the TOA during clear-sky conditions; a first-order approximation as to when the TOA net CRF can be negative. The sign and magnitude of the net CRF hinges on the interaction between a host of different cloud and environmental properties; including surface albedo, solar zenith angle (SZA), COD, cloud top temperature, and cloud D_e. Monthly mean surface albedos are constrained in our calculations by the CERES SYN1deg version 4A product (Wielicki et al. 1996). The intra-annual variability of surface albedo for each site is provided in Fig. 1d along with the annual means. Surface albedos are relatively constant throughout the year at all sites except Fairbanks, where the monthly mean values range from 0.1 during late Spring to early Fall and increase to above 0.3 in the winter when snow is covering the surface.

Ackerman et al. (1988) and Berry and Mace (2014) analyze the change in TOA CRF with COD and ice water path (IWP), respectively, effectively determining whether optically thin or more opaque cirrus have a greater impact on the overall mean CRF. In Section 2c, we follow their methods, thereby highlighting the reponse in daytime TOA net CRF as a function of COD. Accordingly, COD relative frequency distributions (Fig. 3e) at each MPLNET site are shown, revealing what has proven a commonly observed feature of cirrus clouds retrieved from lidar measurements – an exponential increase toward the optically thinnest cloud layers (e.g., Campbell et al. 2015). The annual average COD solved using 20 and 30 sr lidar ratios ranges from 0.11—0.18 and 0.22–0.40, respectively. Vertically-resolved cloud D_e are averaged for each individual cloud profile and binned according to their average size in Fig. 3g. Relative frequency distributions of the average cloud D_e are similar among the sites with peaks between 30 and 45 μm. Annual averages are approximately 40 μm.

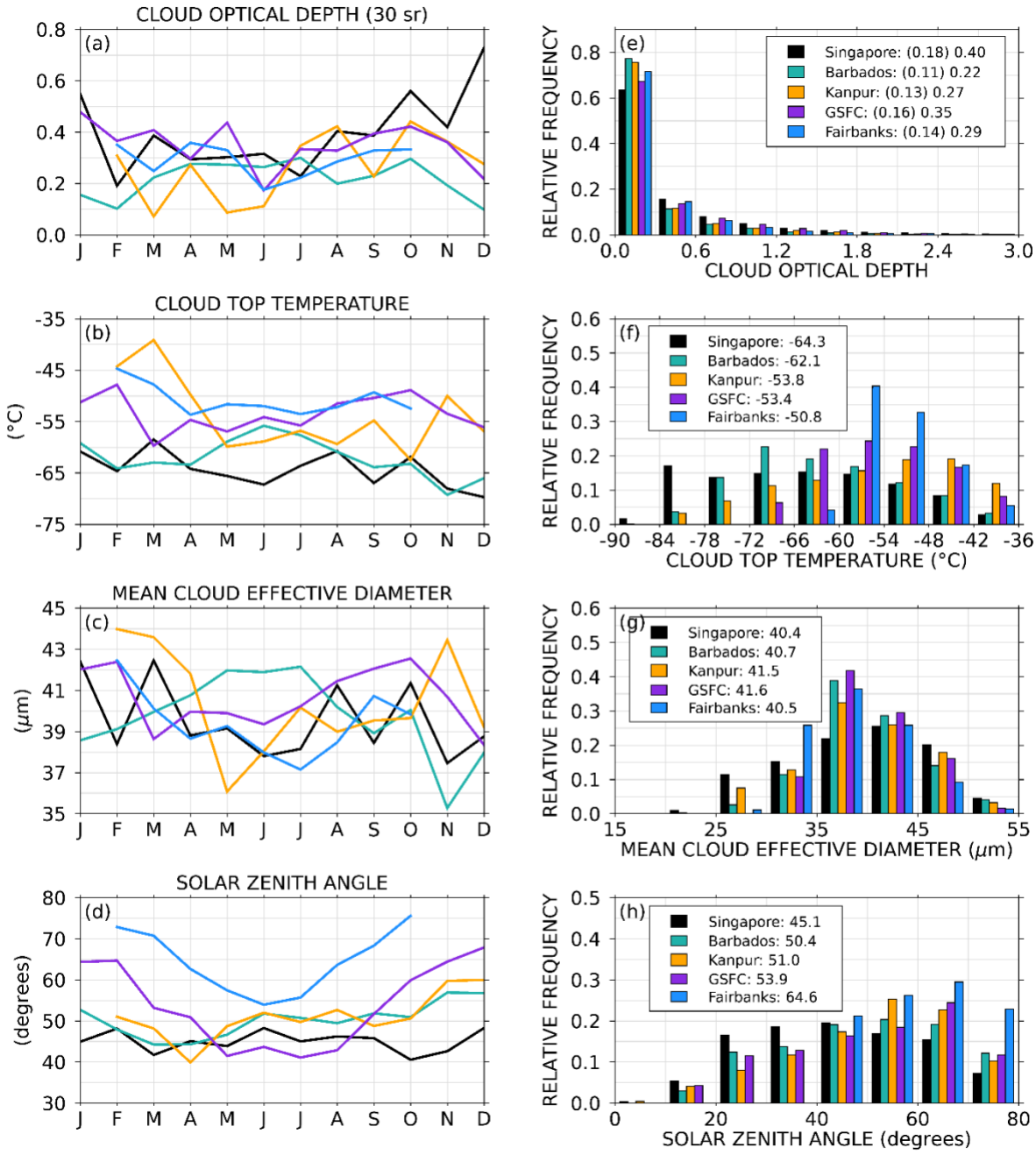


Figure 3: The intra-annual variability in daytime cirrus (a) cloud optical depth (COD; 30 sr), (b) cloud top temperature (°C), (c) mean cloud effective diameter (μm), and (d) solar zenith angle (degrees) at each MPLNET site; Singapore (black), Barbados (green), Kanpur (orange), GSFC (purple), and Fairbanks (blue). Annual relative frequency distributions of the same parameters are given in (e)–(h) with legends containing annual the averages. The COD legend shows the (20 sr) 30 sr value.

Daytime cirrus cloud top temperatures are lowest, on average, at Singapore and Barbados (–64 to –62 °C), and increase by roughly 10 °C at Kanpur and GSFC (Fig. 3f). Cirrus near Fairbanks are the warmest for this selection of sites with an annual average cloud top temperature of

approximately –51 °C. A latitudinal trend in cloud top temperatures is consistent with tropopause height lowering from the equator to the poles (Campbell et al. 2015). Daytime cirrus also tend to be colder during summer months given a similar logic; tropopause heights increase during summertime. Not surprisingy, SZA also has a poleward trend where the sun is more commonly overhead at Singapore (during summer) and more frequently lower on the horizon at Fairbanks (during winter). Their average SZAs are 45.1° and 64.6°, respectively. Recall, the cirrus cloud sample for this study is limited to daytime only, thus there are no data during Arctic winter (i.e., Fig 1a).

b. Instantaneous daytime cirrus cloud radiative forcing

Each cirrus cloud profile is processed individually, yielding profiles of upward and downward SW and LW fluxes. These radiative flux profiles are then used to compute the TOA CRF. At the TOA, CRF is defined as the difference in outgoing flux (F) during clear-sky conditions and when clouds are present:

$$TOA\ CRF_{\lambda} = (F_{\lambda}\uparrow)_{clear} - (F_{\lambda}\uparrow)_{cloud} \quad (1)$$

where λ is the broadband SW or LW (net = SW + LW) value. The nine ice crystal habit optical models, with three levels of particle roughness (27 models in total), are applied in FLG for each individual cirrus cloud profile to estimate the uncertainty of their resulting daytime radiative properties. Additionally, since MPLNET cirrus cloud profile retrievals are constrained by two lidar ratios (20 and 30 sr), the uncertainty is also derived under these two conditions.

The model average daytime TOA CRF is solved for each individual cirrus cloud profile as the average value solved when applying all ice crystal optical models. The absolute uncertainty is calculated as the standard deviation. Throughout the year, the model average instantaneous daytime TOA net CRF regularly switches sign, where roughly 70–90% of the entire sample at each site falls within ±10 $W{\cdot}m^{-2}$ (Fig. S1a). Comparitively, roughly 75–85% (60–80%) of the yearly samples are characteristic of model average instantaneous daytime TOA SW (LW) CRF values between –20–0 $W{\cdot}m^{-2}$ (0–20 $W{\cdot}m^{-2}$) (Fig S1c–1e).

Absolute uncertainties in the instantaneous daytime TOA net CRF are slightly smaller in magnitude compared with the possible range in the model mean, where 75–85% of the cirrus cloud profiles are less than 8 $W{\cdot}m^{-2}$. The fractional uncertainty (i.e., absolute uncertainty divided

by the model mean) in net CRF is tricky to report due to its ability to switch sign, and thus can amount to relatively small values close to zero. Given this method, we see that roughly 20–30% of the total sample is characterized by an uncertainty of greater than 100%, and in some cases even more than 1000%. As such we will refrain from reporting fractional uncertainties and instead report only the absolute uncertainties from here on. As such, the instantaneous daytime TOA SW (LW) CRF has an estimated uncertainty of less than 10 $W \cdot m^{-2}$ (3 $W \cdot m^{-2}$) in 75–90% (70–95%) of all profiles. Model average and absolute uncertainties of the instantaneous daytime cirrus cloud TOA net, SW, and LW CRFs are averged monthly and reported in Tables S1–S3.

c. Absolute daytime cirrus CRF

The absolute daytime TOA CRF is broadly defined as the contribution of daytime cirrus clouds to the total planetary radiation budget. First, we calculate the normalized daytime TOA CRF $\left(\widetilde{CRF}\right)$ as:

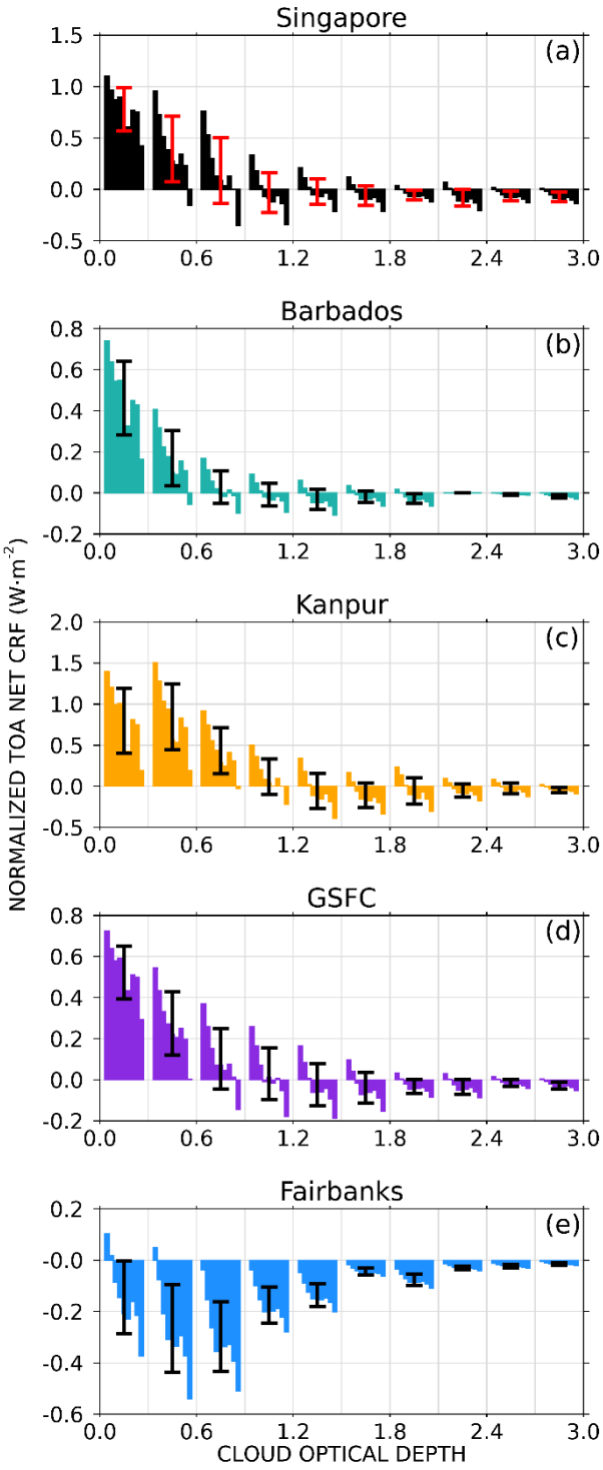
$$\widetilde{CRF} = \overline{CRF_i} \times RF_i \times CF \times DF \quad (2)$$

where $\overline{CRF_i}$ is the averaged TOA net CRF and RF_i is the cloud relative frequency (e.g., Fig. 3e) solved at discrete COD bins (i). Cloud fraction (CF; Fig. 1b) is estimated based on 15 years of global satellite lidar measurements from the Cloud Aerosol Lidar with Orthogonal Polarization (CALIOP) (Vaughan et al. 2009; Winker et al. 2009). Daytime fraction (DF; Fig. 1c) is computed based on broadband SW and LW fluxes that are bound by climatological meteorological conditions; again, under the assumption that daytime hours are those when the incoming TOA net clear-sky flux exceeds that of the corresponding outgoing flux. The intra-annual variability of CF and DF, as well as their annual averages, are provided in Fig. 1. Intergrating $\widetilde{CRF}$ then gives you the absolute daytime TOA CRF:

$$Absolute\ daytime\ TOA\ CRF = \sum_{COD=0}^{3} \widetilde{CRF} \quad (3)$$

The normalized daytime TOA net CRF at each site is shown in Fig. 4. Each COD bin contains results from the nine ice crystal optical models, averaged for particle roughness. There is a

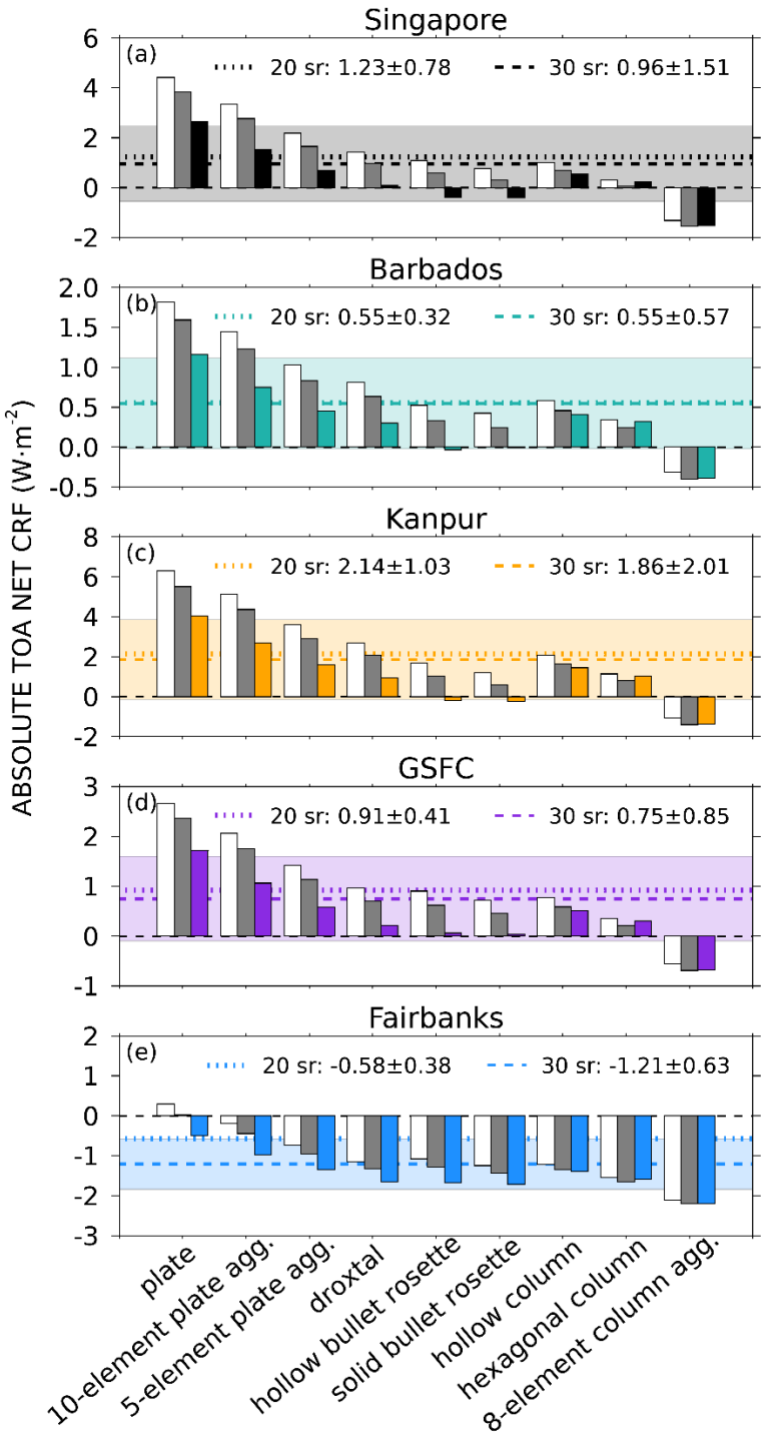
notable sensitivity in the normalized daytime TOA net CRF to ice crystal shape at all sites. At all sites except Fairbanks, the smallest COD bins (i.e., COD < 0.9) result in a positive average TOA net CRF during August, on average, for all nine ice crystal shapes. Fairbanks is unique in this case because SZAs and cloud top temperatures are much larger and warmer, respectively, than those occurring at other the sites. As a result, the SW albedo and LW greenhouse effects are relatively stronger and weaker, respectively. While the daytime TOA net CRF transitions to a negative value as clouds become optically thicker, the COD value at which this transition occurs is unique to each site and ice crystal shape. Additionally, the normalized TOA net CRF, and its relative uncertainty (represented by the error bars), is maximized at the smaller CODs and is driven by the higher relative frequency of optically thinner clouds.



311

312 **Figure 4**: The normalized daytime TOA net CRF (W·m^{-2}) as a function of cloud optical depth (COD; bin size =
313 0.3) at (a) Singapore, (b) Barbados, (c) Kanpur, (d) GSFC, and (e) Fairbanks. The nine bars within each COD bin
314 are the values calculated based on the nine ice crystal optical models, averaged over the three particle
315 roughness's. Error bars represent the standard deviation of the nine values within each COD bin. Results are
316 for August and based on an assumed lidar ratio of 30.

317 The absolute daytime TOA net CRF is then solved with respect to the nine ice crystal shapes
318 (and roughnesses) and shown in Fig. 5. On average during August, the absolute daytime TOA net
319 CRF is positive at all sites except Fairbanks (–1.21 to –0.58 $W \cdot m^{-2}$). Kanpur exhibits the largest
320 monthly average positive TOA net CRF (i.e., greenhouse effect; 1.86–2.14 $W \cdot m^{-2}$), followed by
321 Singapore (0.96–1.23 $W \cdot m^{-2}$), GSFC (0.75–0.91 $W \cdot m^{-2}$), and Barbados (0.55 $W \cdot m^{-2}$). Furthermore,
322 the absolute daytime TOA net CRF is physically consistent with relatively stronger forward
323 scattering for plate-like ice crystals and decreases for bullet rosettes and columns – a similar
324 relationship to the decrease in asymmetry factor with particle habit (i.e., Fig. 2c–2d). The 8-
325 element column aggregate (plate) model consistently produces the strongest negative (positive)
326 absolute daytime TOA net CRF and the result falls outside the bounds of the standard deviation
327 for all sites.



328

329 **Figure 5**: The absolute daytime TOA net CRF ($W \cdot m^{-2}$) solved based on each of the nine optical models at (a)
330 Singapore, (b) Barbados, (c) Kanpur, (d) GSFC, and (e) Fairbanks. Different colors indicate the varying levels of
331 ice crystal particle roughness; smooth (white), moderate (grey), and severe (color). The colored horizontal
332 dashed lines are the average of all optical models while the shaded area represents the standard deviation.
333 Monthly averages and standard deviations are listed in the legend of each panel. Results are for August and
334 based on an assumed lidar ratio of 30. The horizontal dotted line is the average based on an assumed lidar
335 ratio of 20 sr.

Ren et al. (2021) similarly investigate the impact of ice crystal optics to CRF estimates in the equatorial western Pacific. They consider three optical libraries from the widely used Fu scheme (Fu 1996; Fu et al. 1998), the 8-element column aggregate shown here, and a new two-habit model (THM; Loeb et al. 2018). Their results are consistent with those here, in that, optical models that induce relatively strong forward scattering scattering (i.e., Fu and plate-like ice crystals), or relatively large asymmetry factors, have the weakest albedo effect. For reference, the THM assumes a mixture of roughened single hexagonal columns and 20-column aggregates. Furthermore, their study shows differences in instantaneous TOA SW and LW CRFs of up to 60 and 6 $W \cdot m^{-2}$, respectively, and is consistent with the results found in this study.

The absolute uncertainty in daytime absolute TOA net CRF of cirrus, based solely on ice crystal single-scattering properties, is defined as the standard deviation among all the models shown in Fig. 5; those standard deviations range from 0.32–0.57 at Barbados to 1.03–2.01 $W \cdot m^{-2}$ at Kanpur. These uncertainties reveal the stark reality that ice crystal shape has an immense effect on the estimated absolute daytime TOA net CRF. Monthly model average absolute daytime TOA net CRF and the estimated uncertainties are provided in Table 1.

$W \cdot m^{-2}$	Singapore		Barbados		Kanpur		GSFC		Fairbanks	
	$\overline{CRF}$	$\sigma(CRF)$	$\overline{CRF}$	$\sigma(CRF)$	$\overline{CRF}$	$\sigma(CRF)$	$\overline{CRF}$	$\sigma(CRF)$	$\overline{CRF}$	$\sigma(CRF)$
January	2.24	2.42	0.20	0.15	-----	-----	-1.86	0.89	-----	-----
February	2.04	0.78	0.24	0.06	0.31	0.35	-1.52	0.78	-0.17	0.05
March	3.00	1.61	0.98	0.38	0.19	0.05	0.13	0.82	-0.53	0.18
April	1.69	1.37	2.51	0.97	0.34	0.13	0.65	0.85	-0.76	0.64
May	2.85	1.48	1.39	1.07	0.14	0.03	1.29	1.39	-0.83	0.79
June	1.02	1.35	0.04	1.30	1.04	0.40	1.00	0.57	0.21	0.50
July	1.27	0.92	0.18	0.72	1.82	1.72	1.58	0.90	-0.36	0.75
August	0.96	1.51	0.55	0.57	1.86	2.01	0.75	0.85	-1.21	0.63
September	1.60	1.65	0.37	0.90	0.58	0.55	0.14	0.48	-1.34	0.54
October	2.89	3.00	0.37	1.03	0.53	0.14	-0.78	0.78	-1.07	0.29
November	3.16	2.18	0.02	0.40	0.23	0.13	-1.05	0.66	-----	-----
December	0.54	3.30	0.30	0.18	0.07	0.10	-1.00	0.51	-----	-----
Annual	1.94	1.80	0.59	0.64	0.65	0.51	-0.06	0.79	-0.67	0.49

Table 1: The monthly average ($\overline{CRF}$) and absolute uncertainty ($\sigma(CRF)$) of absolute daytime TOA net CRF ($W \cdot m^{-2}$) computed based on the nine ice crystal habit optical models. Results are shown for an assumed lidar ratio of 30 sr. The annual values reported here are roughly 1.7–2.0 times larger than those estimated using a lidar ratio of 20 sr.

Another noteworthy feature of these results is that the absolute daytime TOA net CRF is more sensitive to roughness for bullet rosettes and plate-like ice crystals than it is for columnar ice crystals or aggregates of columns. Justifiably, the average standard deviations in absolute daytime TOA net CRF with respect to ice crystal relative particle roughness for 10-element plate aggregates, solid bullet rosettes, and 8-element column aggregates are 0.36–0.69, 0.29–0.54, and 0.05–0.09 $W \cdot m^{-2}$ (66, 41, and 9%), respectively, across all sites.

The intra-annual variability in absolute daytime TOA net CRF is shown in Fig. 6. Tropical sites (e.g., Singapore, Barbados, and Kanpur) do not have a clear seasonal cycle and the monthly means remain positive throughout the year. The indistinct seasonal cycle at the tropical sites is a reflection of rather weak intra-annual signals of their cloud and environmental properties (i.e., Fig. 1 and Fig. 3). However, the notable jump in TOA net CRF at Kanpur during the summer months corresponds to an increase in CF (i.e., Fig. 1b). Analysis over multiple years would provide more context about the true seasonal cycles at the tropical sites.

Furthermore, the variance in absolute daytime TOA net CRF, due to the nine ice crystal optical models, suggests the sign can change throughout the year. There are also months without consensus, meaning the sign of the monthly mean TOA net CRF could be either positive or negative; for example, May through November at Barbados. The absolute daytime TOA net CRF does change sign throughout the year at GSFC where the montly average is negative during winter and positive during summer. Fairbanks experiences a similar changeover in sign, where the absolute daytime TOA net CRF is positive in June and negative in all other months with sufficient sunlight.

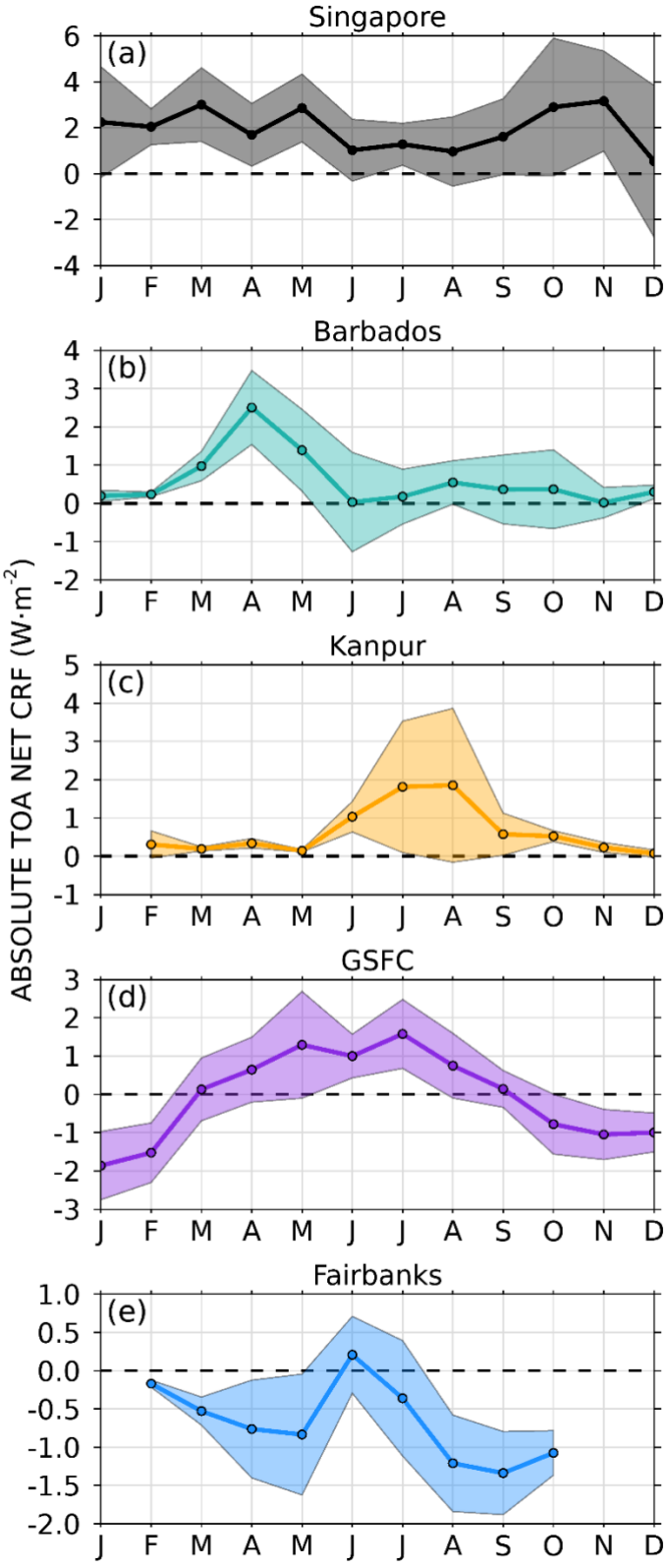


Figure 6: Annual variations of the [30 sr] absolute daytime TOA net CRF ($W \cdot m^{-2}$) at (a) Singapore, (b) Barbados, (c) Kanpur, (d) GSFC, and (e) Fairbanks. Solid lines are the monthly average and shaded areas are the standard deviation (i.e., fractional uncertainty) based on all optical models (as in Fig. 5).

Absolute uncertainties in the annual mean absolute daytime TOA net CRF range from approximately 0.5–1.8 $W \cdot m^{-2}$, while fractional uncertainties range form 40–130%, on average. GSFC is an outlier where the annual mean fractional uncertainty is more than 1000%, however, this is due to a very small monthly mean value (–0.06 $W \cdot m^{-2}$) and a reasonable absolute uncertainty (0.79 $W \cdot m^{-2}$). Again, this method for calculating uncertainty can skew interpretation given that the net CRF commonly changes sign. Uncertainties in the annual mean absolute daytime TOA SW and LW CRF are approximately 21.5% and 6.8%, respectively. The SW and LW CRF monthly model averages and absolute uncertainties are provided in Table S4–S5.

Since operational radiative transfer codes require input of the ice crystal particle size for estimating the cloud single-scattering properties, we found it useful to design a simple experiment to determine which assumption leads to greater uncertainty in the absolute daytime TOA net CRF: the underlying single-scattering properties or the parameterization for estimating ice crystal particle size? The experiment takes into account combinations of the D22 and Heymsfield et al. (2014) (hereafter H14) parameterization for solving ice crystal D_e and the 8-element column aggregate (8CA) and Yang et al. (2000; 2005) optical models, an option that comes standard in FLG. D22 relates temperature and extinction coefficient to effective particle size and is derived from globally distributed optically thin to opaque ice clouds from combined satellite radar and lidar measurements. H14 aggregates globally distributed in-situ aircraft measurements of ice clouds to form a parameterized solution for effective size that also depends on temperature and extinction. The four experiments are defined with the following combinations: (1) D22 and 8CA-severely roughened; (2) H14 and 8CA-severely roughened; (3) D22 and Yang (2000; 2005); (4) H14 and Yang (2000; 2005).

Figure 7 shows the annual mean absolute daytime TOA net CRF of cirrus based on the 20 and 30 sr lidar solutions. Experiment 4 produces a positive value at every site for both the 20 and 30 sr solutions (except at Fairbanks: –0.01 $W \cdot m^{-2}$). Experiment 1 is consistent with weaker forward scattering where the daytime TOA net CRF is weakest overall; either a relatively weak positive value or relatively strong negative value. Experiment 1 is also the only one to consistently fall outside the variance in annual mean absolute daytime TOA net CRF resulting from the nine optical models. The absolute daytime TOA net CRF generally decreases from the equator to the

poles, as hypothesized and shown in Campbell et al. (2016), Lolli et al. (2017), and Campbell et al. (2021). When holding optics constant (Experiment 1 vs 2), there is a difference of 0.12–0.25 $W \cdot m^{-2}$ in the TOA net CRF, however, when holding D_e constant (Experiment 3 vs 4) the average difference is 0.57–0.99 $W \cdot m^{-2}$. Therefore, based on this analysis, we can generally conclude that the absolute daytime TOA net CRF is more sensitive to ice cloud single-scattering properties than it is to parameterized D_e for daytime cirrus radiative forcing studies. For reference, the D14 parameterization produces mean cloud D_e that are 30–130 µm larger than those solved with D22.

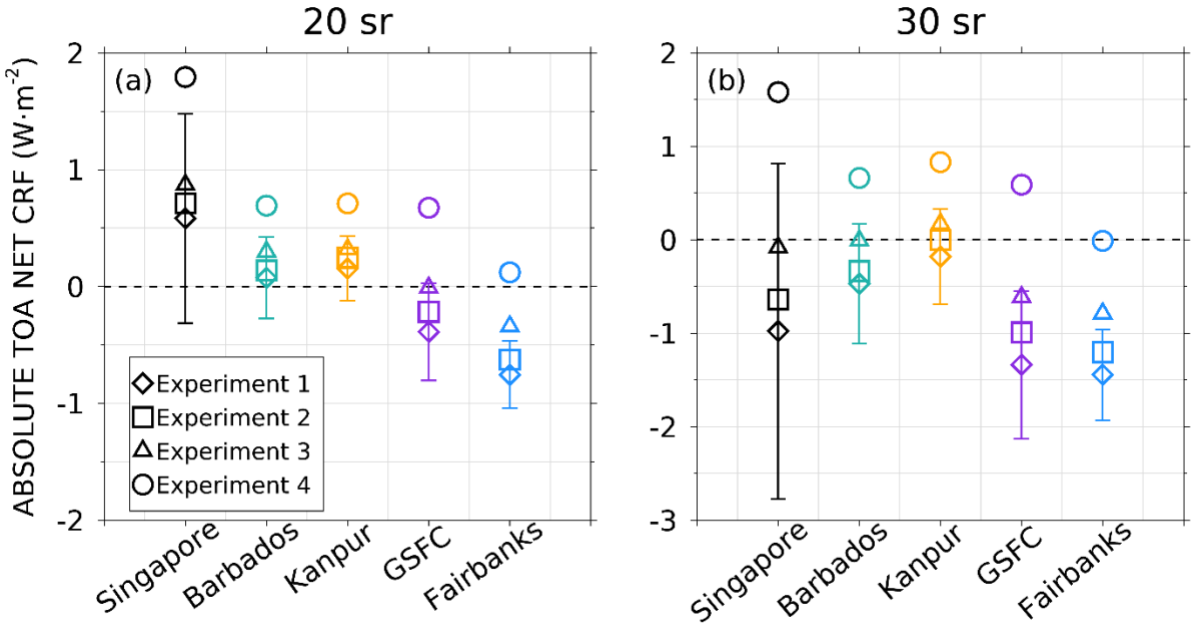


Figure 7: The annual mean absolute daytime TOA net CRF at (a) 20 sr and (b) 30 sr for cirrus clouds at the five MPLNET sites. Each symbol represents a different experiment depending on which combination of effective diameter parameterization and ice cloud optical model is used to solve radiative transfer. Experiment 1 (diamond) – D22 and 8CA-severely roughened; Experiment 2 (square) – H14 and 8CA-severely roughened; Experiment 3 (triangle) – D22 and Yang (2000; 2005); Experiment 4 (circle) – H14 and Yang (2000; 2005). Error bars associated with Experiment 1 are the standard deviation in absolute CRF computed based on the nine ice crystal optical models.

d. Cirrus cloud radiative heating rates

The uncertainties in daytime cirrus cloud radiative heating rate profiles are also estimated at the five MPLNET sites. The net, SW, and LW radiative heating rates are isolated *within* cloud layers to determine their sensitivity to ice cloud optical single-scattering properties. Cloud layers are converted into fractional layers, or a normalized cloud height, in 10% increments to create a consistent and uniform analysis of the cloud radiative heating rates that are not tied to

differences in cloud thickness or vertical placement. The instantaneous cloud radiative heating rate profiles are averaged monthly under the assumption they occur during daytime.

Figure 8 depicts the vertical variation of daytime in-cloud radiative heating rates of semi-transparent cirrus clouds at the five MPLNET sites during August. On average, the cirrus cloud net radiative heating rates are largest at Kanpur with a maximum value near +7 K/day, are similar in magnitude at Singapore, Barbados, and GSFC; all peaking around +4 K/day, and are smallest at Fairbanks with a maximum value near +1 K/day. Overall, the net radiative heating rates are positive and peak within the middle third of the cloud layer. Fairbanks is the only site with net cloud-top cooling, on average. However, one of the ice crystal habit models does produce negative cloud-top cooling at GSFC (not shown). Monthly model mean vertical net radiative heating rates and absolute uncertainties profiles are further averaged through the entire cloud layer and are provided in Table 2.

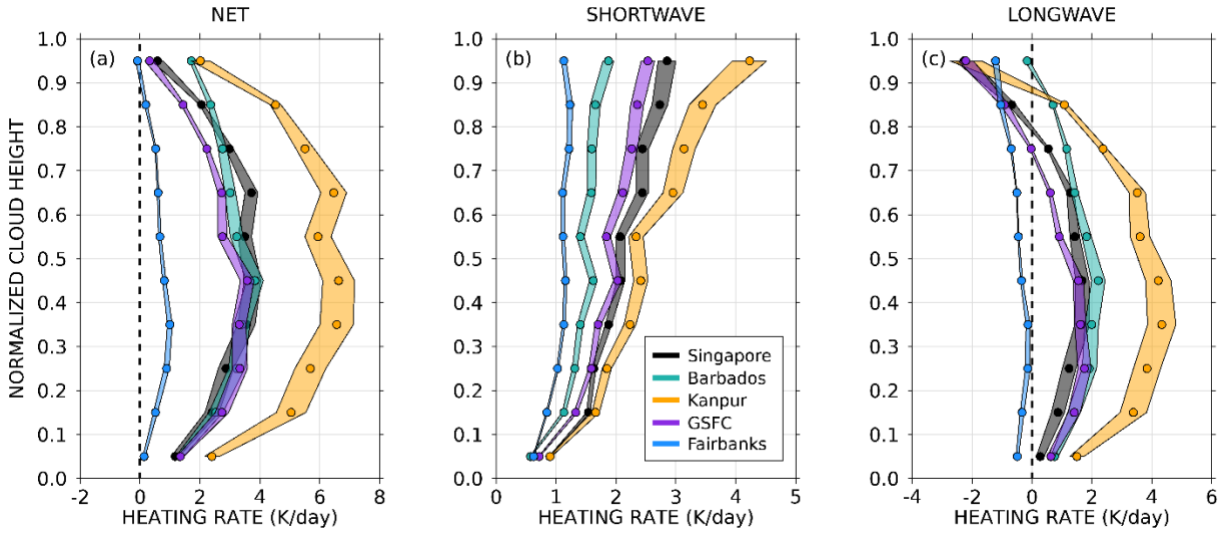


Figure 8: Average instantaneous in-cloud daytime (a) net, (b) SW, and (c) LW radiative heating rates during August at each MPLNET site. Heating rates are binned at 10% vertical fractional levels within the cloud layer. Shaded areas represent the standard deviation (i.e., absolute uncertainty) of radiative heating across the nine different ice crystal shapes. Results are based on an assumed lidar ratio of 30 sr.

On average, instantaneous SW heating rates (Fig. 8b) are positive throughout the cloud layer and increase is magnitude from cloud base to the cloud top. Again, Kanpur exhibits the strongest relative radiative heating (+4 K/day) among the five sites while Fairbanks has the weakest (+1 K/day). At Singapore, Barbados, Kanpur, and GSFC, the average LW heating rates are positive

through the bottom 70-90% of the cloud layer and transition to a negative value near the cloud top. Daytime cirrus clouds at Fairbanks induce LW cooling through the entire cloud layer, on average. We acknowlege that the average net radiative heating rate reported for Kanpur is relatively large during October (~10 K/day), however, the sample is small (80 total) and may not be representative of the entire month. Monthly statistics for the SW and LW radiative heating rates are similarly provided in Tables S6–S7.

K/day	Singapore		Barbados		Kanpur		GSFC		Fairbanks	
	$\overline{Q_r}$	$\sigma(Q_r)$	$\overline{Q_r}$	$\sigma(Q_r)$	$\overline{Q_r}$	$\sigma(Q_r)$	$\overline{Q_r}$	$\sigma(Q_r)$	$\overline{Q_r}$	$\sigma(Q_r)$
January	3.96	0.29	3.69	0.32	-----	-----	1.03	0.12	-----	-----
February	2.86	0.20	2.64	0.19	1.65	0.13	0.44	0.09	-0.76	0.07
March	4.31	0.29	3.44	0.24	0.37	0.03	2.31	0.16	-0.53	0.02
April	3.38	0.26	3.67	0.25	2.36	0.15	1.98	0.14	0.46	0.06
May	3.95	0.30	2.73	0.19	2.74	0.27	2.94	0.20	0.72	0.06
June	3.62	0.28	2.02	0.15	1.76	0.15	1.63	0.10	0.77	0.05
July	2.24	0.17	2.42	0.16	3.63	0.29	3.34	0.22	0.97	0.07
August	2.66	0.20	2.74	0.19	5.08	0.40	2.38	0.16	0.52	0.05
September	3.51	0.26	2.58	0.18	1.90	0.16	2.55	0.18	0.50	0.07
October	4.94	0.38	3.00	0.20	10.69	0.74	1.52	0.13	-0.42	0.04
November	5.90	0.47	2.36	0.19	5.25	0.34	0.89	0.09	-----	-----
December	4.75	0.36	1.74	0.15	2.24	0.17	0.58	0.06	-----	-----
Annual	3.84	0.29	2.75	0.20	3.43	0.26	1.80	0.14	0.25	0.06

Table 2: The monthly average ($\overline{Q_r}$) and absolute uncertainty ($\sigma(Q_r)$) of average in-cloud net radiative heating rates (Q_r; K/day) computed based on the nine ice crystal habit optical models. Results are shown for an assumed lidar ratio of 30 sr. The annual values reported here are roughly 1.6–2.1 times larger than those estimated using a lidar ratio of 20 sr.

Vertical profiles of radiative heating rate absolute uncertainty are explicitly shown in Fig. 9. In general, the magnituide of absolute uncertainty is maximized in layers that have relatively large radiative heating rates. For example, both the LW and net radiative heating absolute uncertainties are largest in the mid-cloud layers and at the cloud top, whereas the uncertainties are relatively small near the cloud base and in upper cloud layers where the radiative heating rates change sign. Alternatively, SW heating rate absolute uncertainties increase from cloud base to cloud top. During August, the largest net radiative heating rate uncertainties are estimated at Kanpur (0.40 K/day), the smallest are at Fairbanks (0.05 K/day), and Singapore, Barbados, and GSFC are roughly in the middle (0.16 – 0.20 K/day).

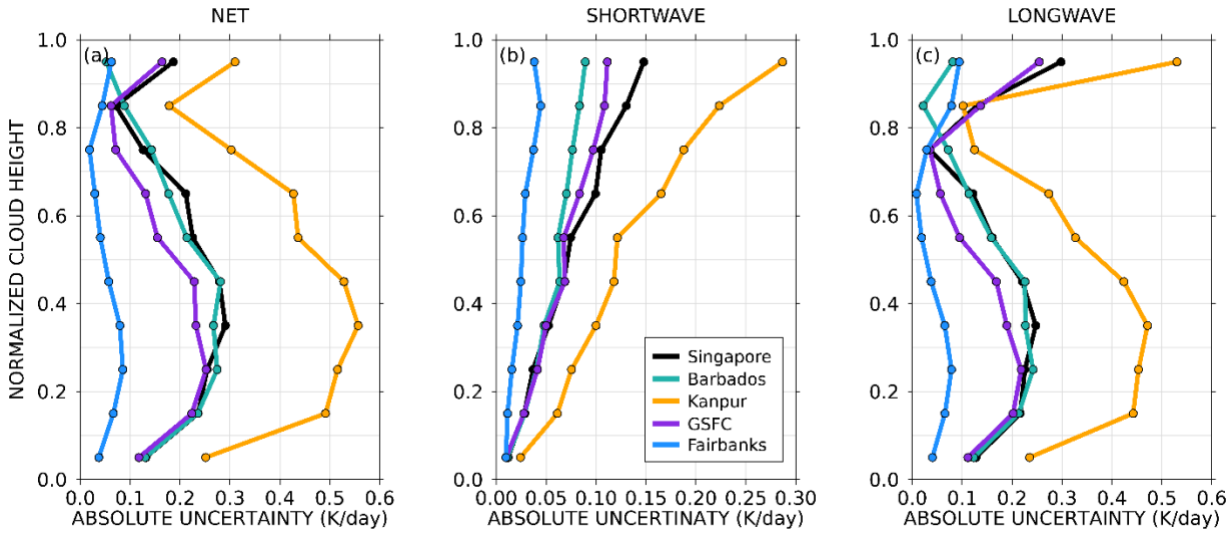


Figure 9: As in Figure 8 but showing only the vertical profiles of daytime cirrus cloud radiative heating rate absolute uncertainty (K/day).

IV. Conclusions

One year of data from five Micro-Pulse Lidar Network (MPLNET) sites spanning the northern hemisphere tropics to high-latitudes are analyzed to derive an estimate of the uncertainty in daytime top-of-the-atmosphere (TOA) cirrus cloud radiative forcing (CRF) and radiative heating rates. This uncertainty is tied to the assumptions related to ice crystal scattering and absorption by way of their optical properties for various particle habits. Cirrus are unique compared with other cloud types because, depending on a host of parameters such as cloud physical and optical properties, surface albedo, and solar geometry, they are the only cloud genus that can regularly induce both a positive or negative effects on the TOA radiation budget during daytime. Yang et al. (2013) and Bi and Yang (2014; 2017) provide libraries of the single-scattering properties for nine different ice crystal shapes (i.e. habits) with varying degrees of particle surface roughness derived from numerical methods. Herein, those optical libraries are integrated within the Fu-Liou-Gu radiative transfer model and applied to lidar measurements of cirrus with cloud optical depth (COD) less than 3.0 and cloud top temperatures less than –37 °C.

All nine ice crystal habits are assumed a reasonable and legitimate option for representing the single-scattering properties of cirrus clouds. As such, when averaged across all habits, the average annual absolute daytime TOA net CRF is positive at Kanpur, Barbados, and Singapore

(0.59–0.67, 0.61–0.65, and 1.94–2.09 $W \cdot m^{-2}$, respectively), negative at Fairbanks (–0.67 to –0.28 $W \cdot m^{-2}$), and either positive or negative at Goddard Space Flight Center (GSFC) (–0.06 to +0.32 $W \cdot m^{-2}$) depending on which lidar ratio is used to constrain cloud extinction. However, ice crystal habit has a considerable impact on the magnitude and sign of the estimated TOA forcing. Plates tend to produce the largest relative absolute forcing and decreases for bullet rosettes and columns. In other words, the positive forcing solved from applying the optical propties for plates implies thin cirrus lead to a greenhouse effect whereas 8-element column aggregates lead to an albedo effect. The documented relationship between particle habit and absolute forcing follows a similar pattern to the asymmetry factor, where its value is largest for plates and decreases for bullet rosettes and even more for columns.

Uncertainties in daytime cirrus cloud radiative properties are estimated at each MPLNET site as the standard deviation of all possible outcomes when considering the different particle habits individually. Annually, the average uncertainty of the absolute daytime TOA net CRF ranges from ~0.50 $W \cdot m^{-2}$ at Kanpur and Fairbanks to 1.80 $W \cdot m^{-2}$ at Singapore. The uncertainty in instantaneous TOA net CRF is larger (3.5–5.5 $W \cdot m^{-2}$) comparitively.

The ice crystal particle size is also a necessary feature to resolve for cloud radiative transfer. Herein, two solutions for solving ice crystal effective diameter are applied to determine its overall impact to the absolute daytime TOA net CRF and whether the parameterized effective diameter (D_e) or the single scattering properties has a larger impact to the final solution. Here, we demonstrate that the the absolute daytime TOA net CRF is roughly four times more sensitive to the optical model single-scattering properties than it is to the parameterization for D_e for daytime cirrus radiative forcing studies.

The model average and uncertainties in daytime net, shortwave, and longwave radiative heating rate profiles are similarly estimated based on the spread caused by varying the ice crystal single-scattering properties. The net in-cloud radiative heating rates are positive at each site, with Kapur having the largest relative peak value and Fairbanks having the smallest. Fairbanks is also the only site with net cooling near the cloud top, on average. On annual average, the net,

shortwave, and longwave radiative heating rates have an estimated uncertainty ranging from 0.06–0.29, 0.03–0.09, and 0.06–0.23, respectively, when averaged through the cloud layer.

One caveat of this study is that entire cloud layers are assumed to be comprised solely of each single particle habit. In reality, clouds may contain many different crystal habits instantaneously. One option to overcome this limitation is to consider both temperature and ice super saturation (as in Pruppacher and Klett 1997) when applying optical properties to account for ice crystal inhomogeneity. We must also acknowledge that the optical property libraries provided from Yang et al. (2013) and Bi and Yang (2014; 2017) are based on idealized ice crystal geometries that may be much simpler compared to realistic ice crystals habits in the atmosphere. As such, we advocate for continued effort focusing on robust sampling of ice cloud optics from in-situ and remote sensing retrievals (e.g., Xu et al. 2022; van Diedenhoven et al. 2012; 2013; 2020). Measurements that are collocated with broad spectrum radiation measurements could provide additional constraints to the propagation of radiation through ice clouds with applications to satellite remote sensing, numerical weather prediction, and climate studies.

It is further plausible that machine learning applications tied to such work could eventually replace these static optical models with dynamic single-scattering solutions. Emerging satellite sensors introduce spectral diversity and novel sampling techniques that could benefit from such solutions. Not only do they support long-term monitoring, they also provide suitable training datasets that cover a representative distribution of translucent and increasingly opaque cirrus. Further study along the lines of inquiry can be performed in order to assess potential biases in our experiments, and thus whether or not habit typing with cloud depth is a necessary requirement in the accurate modeling of cloud radiative effects for climate and weather modeling applications. Accordingly, more advanced spectral constraints of cloud properties from satellites continues growing in prominence, as the community more accurately resolves clouds of all types and phases.

Acknowledgements

This study was supported by the Naval Research Laboratory both in the form of a Karle's Research Fellowship for E.K. Dolinar and through the Radiative Effects of Thin Cirrus Clouds (REThinC)

project supported by its Base Program (BE033-03-45-T008-17; Drs. Simon Chang, James Hansen, and Ruth Preller). The Micro-Pulse Lidar Network is supported by the NASA Radiative Sciences Program (J. R. Lewis and E. J. Welton).

Availibitlity Statement

The NASA MPLNET version 3 cloud product data used in this study are available at https://mplnet.gsfc.nasa.gov/download_tool/ and processed according to Lewis et al. (2016). Dr Ping Yang manages the Version 2 ice crystal optical library (Yang et al. 2013; Bi and Yang 2014; 2017) at https://zenodo.org/record/5348402#.ZFFkvHbMJX1 (https://doi.org/10.1175/JAS-D-12-039.1). The Fu-Liou-Gu (FLG) radiation transfer model (RTM) is based on Gu et al. (2003). Figures and a wrapper for the FLG RTM were developed using the Interactive Data Language (IDL), with licensing purchased by the Naval Research Laboratory.

References

Ackerman, T.P., Liou, K.-N., Valero, F.P.J., and Pfister, L. (1988). Heating Rates in Tropical Anvils. *J. Atmos. Sci*., 45, 1606–1623, https://doi.org/10.1175/1520-0469(1988)045<1606:HRITA>2.0.CO;2.

Bailey, M.P., and Hallett, J. (2009). A Comprehensive Habit Diagram for Atmospheric Ice Crystals: Confirmation from the Laboratory, AIRS II, and Other Field Studies, *J. of the Atmos. Sci.,* 66(9), 2888-2899.

Baran, A.J. (2009). A review of the light scattering properties of cirrus. *J. of Quant. Spectro.and Rad. Trans., 110*(14-16), 1239-1260. https://doi.org/10.1016/j.jqsrt.2009.02.026.

Baumgardner, D., Abel, S.J., Axisa, D., Cotton, R., Crosier, J., Field, P., Gurganus, C., Heymsfield, A., Korolev, A., Krämer, M., Lawson, P., McFarquhar, G., Ulanowski, Z., and Um, J. (2017). Cloud Ice Properties: In Situ Measurement Challenges, *Meteorological Monographs*, 58, 9.1-9.23

Berry, E., and Mace, G.G. (2014). Cloud properties and radiative effects of the Asian summer monsoon derived fromA-Train data, *J. Geophys. Res. Atmos*., 119,9492–9508, doi:10.1002/2014JD021458.

Bi, L., and Yang, P. (2014). Accurate simulation of the optical properties of atmospheric ice crystals with the invariant imbedding T-matrix method. *J. of Quant. Spectrosc. and Radiat. Trans.*, *138*, 17-35.

Bi, L., and Yang, P. (2017). Accurate simulation of the optical properties of atmospheric ice crystals with invariant imbedding T-matrix method. *J. Quant. Spectrosc. Radiat. Trans*., 138, 17–35, https://doi.org/10.1016/j.jqsrt.2014.01.013.

Bonan, D.B., Armour, K.C., Roe, G.H., Siler, N., and Feldl, N. (2018). Sources of uncertainty in the meridional pattern of climate change. *Geophys. Res. Lett.*, 45, 9131–9140. https://doi.org/10.1029/2018GL079429.

Campbell, J.R., Hlavka, D.L., Welton, E.J., Flynn, C.J., Turner, D.D., Spinhirne, J.D., Scott, V.S., and Hwang, I.H. (2002). Full-Time, Eye-Safe Cloud and Aerosol Lidar Observation at Atmospheric Radiation Measurement Program Sites: Instruments and Data Processing. *J. Atmos. Oceanic Technol.*, 19, 431–442, https://doi.org/10.1175/1520-0426(2002)019<0431:FTESCA>2.0.CO;2.

Campbell, J.R., Sassen, K., and Welton, E.J. (2008). Elevated cloud and aerosol layer retrievals from micropulse lidar signal profiles. *J. Atmos. Oceanic Technol*., 25, 685–700, https://doi.org/10.1175/2007JTECHA1034.1.

Campbell. J.R., Vaughan M.A., Oo, M., Holz, R.E., Lewis, J.R., and Welton, E.J. (2015). Distinguishing cirrus cloud presence in autonomous lidar measurements. *Atmos. Meas. Tech*., 8, 435–449, https://doi.org/10.5194/amt-8-435-2015.

Campbell, J.R., Lolli, S., Lewis, J.R., Gu, Y., and Welton, E.J. (2016). Daytime cirrus cloud top-of-atmosphere radiative forcing properties at a midlatitude site and their global consequence. *J. Appl. Meteor. Climatol.,* 55, 1667–1679, https://doi.org/10.1175/JAMC-D-15-0217.1.

Campbell, J.R., Dolinar, E.K., Lolli, S., Fochesatto, G.J., Gu, Y., Lewis, J.R., Marquis, J.W., McHardy, T.M., Ryglicki, D.R., and Welton, E.J. (2021). Cirrus Cloud Top-of-the-Atmosphere Net Daytime Forcing in the Alaskan Subarctic from Ground-Based MPLNET Monitoring, *J. of Appl. Meteor. Climatol.,* 60(1), 51-63, https://doi.org/10.1175/JAMC-D-20-0077.1.

Crueger, T., and Stevens, B. (2015). The effect of atmospheric radiative heating by clouds on the Madden–Julian Oscillation. *J. Adv. Model Earth Syst.,* 7:854–864. https://doi.org/10.1002/2015M S0004 34.

Dolinar, E.K., Dong, X., Xi, B., Jiang, J.H., Loeb, N.G, Campbell, J.R, and Su, H. (2019) A global record of single-layered ice cloud properties and associated radiative heating rate profiles from an A-Train perspective. *Clim. Dyn.,* 53, 3069–3088, https://doi.org/10.1007/s00382-019-04682-8.

Dolinar, E.K., Campbell, J.R., Marquis, J.W., Garnier, A.E., and Karpowicz, B.M. (2022). Novel Parameterization of Ice Cloud Effective Diameter from Collocated CALIOP-IIR and CloudSat Retrievals, *J. of Appl. Meteo. and Clim*., 61(7), 891-907.

Fu, Q., and Liou, K.N. (1992). On the correlated *k*-distribution method for radiative transfer in nonhomogeneous atmospheres. *J. Atmos. Sci*, 49, 2139–2156.

Fu, Q., and, Liou, K.-N. (1993). Parameterization of the radiative properties of cirrus clouds. *J. Atmos. Sci*, 50, 2008–2025.

Fu, Q. (1996). An accurate parameterization of the solar radiative properties of cirrus clouds for climate models. *J. Climate*, 9, 2058–2082, https://doi.org/10.1175/1520-0442(1996)009<2058:AAPOTS>2.0.CO;2.

Fu, Q., Yang, P., and Sun, W. (1998). An accurate parameterization of the infrared radiative properties of cirrus clouds for climate models. *J. Climate*, 11, 2223–2237, https://doi.org/10.1175/1520-0442(1998)011<2223:AAPOTI>2.0.CO;2.

Gu, Y., Farrara, J., Liou, K.N., and Mechoso, C.R. (2003). Parameterization of cloud-radiation processes in the UCLA general circulation model. *J. Climate*, 16, 3357–3370.

Gu, Y., Liou, K.-N., Ou, S.C., and Fovell, R. (2011). Cirrus cloud simulations using WRF with improved radiation parameterization and increased vertical resolution. *J. Geophys. Res*, 116, D06119, doi: 10.1029/2010JD014574.

Harrop, B.E., Hartmann DL (2016). The role of cloud radiative heating in determining the location of the ITCZ in aquaplanet simulations. J Clim 29:2741–2763. https ://doi.org/10.1175/JCLI-D-15-0521.1.

Havemann, H., and Baran, A.J. (2001). Extension of T-matrix to scattering of electromagnetic plane waves by non-axisymmetric dielectric particles: application to hexagonal ice cylinders *J. Quant. Spectrosc. Radiat. Transf*., 70, 139-158.

633 Jahangir, E., Libois, Q., Couvreux, F., Vié, B., and Saint-Martin, D. (2021). Uncertainty of SW cloud
634 radiative effect in atmospheric models due to the parameterization of liquid cloud optical
635 properties. *Journal of Advances in Modeling Earth Systems*, 13,
636 e2021MS002742. https://doi.org/10.1029/2021MS002742.
637 Järvinen, E., Vochezer, P., Möhler, O., Schnaiter, M. (2014). Laboratory study of microphysical
638 and scattering properties of corona-producing cirrus clouds", *Applied Optics*, 53, 7566-7575.
639 Järvinen, E., Wernli, H., Schnaiter, M. (2018). Investigations of mesoscopic complexity of small
640 ice crystals in mid-latitude cirrus, *Geophys. Res. Lett*., 45, doi.org/10.1029/2018GL079079.
641 Lewis, J.R., Campbell, J.R., Welton, E.J., Stewart, S.A., and Haftings, P.C. (2016). Overview of
642 MPLNET, version 3, cloud detection. *J. Atmos. Oceanic Technol.,* 33, 2113–2134,
643 https://doi.org/10.1175/JTECH-D-15-0190.1.
644 Lin, J., Mapes, B., Zhang, M., and Newman, M. (2004). Stratiform Precipitation, Vertical Heating
645 Profiles, and the Madden–Julian Oscillation. *J. Atmos. Sci*., 61, 296–309,
646 https://doi.org/10.1175/1520-0469(2004)061<0296:SPVHPA>2.0.CO;2.
647 Liou, K.N, and Yang, P. (2016). *Light Scattering by Ice Crystals*. Cambridge University Press.
648 Loeb, N.G., and Coauthors (2018). Impact of ice cloud microphysics on satellite cloud retrievals
649 and broadband flux radiative transfer model calculations. *J. Climate*, 31, 1851–
650 1864, https://doi.org/10.1175/JCLI-D-17-0426.1.
651 Lolli, S., Campbell, J.R., Lewis, J.R., Gu, Y., Marquis, J.W., Chew, B.N., Liew, S-C, Salinas, S.V., and
652 Welton, E.J. (2017). Daytime top-of-the-atmosphere cirrus cloud radiative forcing properties
653 at Singapore. *J. Appl. Meteor. Climatol*., 56, 1249–1257, https://doi.org/10.1175/JAMC-D-16-
654 0262.1.
655 Macke, A., Mishchenko, M.I., Muinonen, K., and Carlson, B.E. (1995). Scattering of light by large
656 nonspherical particles: ray tracing approximation versus T-matrix method. *Opt. Lett*., 20, 1934-
657 1936.
658 Molod, A., Takacs, L., Suarez, M., Bacmeister, J., Song, I.-S., and Eichmann, A. (2012). The GEOS-
659 5 atmospheric general circulation model: Mean climate and development from MERRA to
660 Fortuna, NASA Tech. Rep. Series on Global Modeling and Data Assimilation, NASA/TM-2012-
661 104606, Vol. 28, NASA Goddard Space Flight Center, 117 pp.

662 Muskatel, H.B., Blahak, U., Khain. P., Levi, Y., and Fu., Q. (2021). Parametrizations of Liquid and
663 Ice Clouds' Optical Properties in Operational Numerical Weather Prediction
664 Models, *Atmosphere* 12, no. 1: 89, https://doi.org/10.3390/atmos12010089.
665 Pruppacher, H.R., and Klett, J.D. (1997). Microphysics of Clouds
666 and Precipitation. Kluwer Academic, 954 pp.
667 Ramanathan, V., Cess, R.D., Harrison, E.F., Minnis, P., Barkstrom, B.R., Ahmad, E., and Hartmann,
668 D. (1989). Cloud-Radiative Forcing and Climate: Results from the Earth Radiation Budget
669 Experiment. *Science,* 243, 57-63.
670 Ren, T., Li, D., Muller, J., and Yang, P. (2021). Sensitivity of Radiative Flux Simulations to Ice Cloud
671 Parameterization over the Equatorial Western Pacific Ocean Region*, J. of the Atmos. Sci*., 78,
672 8, 2549-2571, https://doi.org/10.1175/JAS-D-21-0017.1.
673 Rienecker, M.M., Suarez, M.J., Todling, R., Bacemeister, J., Takacs, L., Liu, H.-C., Gu, W.,
674 Sienkiewicz, M., Koster, R.D., Gelaro, R., Stanjer, I., and Nielsen, J. E. (2008). The GEOS-5 data
675 assimilation system – Documentation of versions 5.0.1, 5.1.0, and 5.2.0, NASA Tech. Rep.
676 Series on Global Modeling and Data Assimilation, NASA/TM-2008-104606, Vol. 27, NASA
677 Goddard Space Flight Center, 101 pp.
678 Rutan, D.A., Kato, S., Doelling, D.R., Rose, F.G., Nguyen, L.T., Caldwell, T.E., and Loeb, N.G. (2015).
679 CERES synoptic product: Methodology and validation of surface radiant flux. *J. Atmos. Oceanic*
680 *Technol*., 32, 1121–1143, https://doi.org/10.1175/JTECH-D-14-00165.1.
681 Stackhouse, P.J. and G.L. Stephens (1991). A Theoretical and Observational Study of the Radiative
682 Properties of Cirrus: Results from FIRE 1986. *J. Atmos. Sci*., **48**, 2044-2059.
683 Stegmann, P.G., Tropea, C., Järvinen, E., Schnaiter, M. (2016). Comparison of measured and
684 computed phase functions of individual tropospheric ice crystals, *J. of Quant. Spectro. and Rad.*
685 *Trans.,* http://dx.doi.org/10.1016/j.jqsrt.2015.12.019.
686 Stevens, B., and Schwartz, S.E. (2012). Observing and Modeling Earth's Energy Flows. *Surv.*
687 *Geophys.,* **33**, 779–816, https://doi.org/10.1007/s10712-012-9184-0.
688 Stubenrauch, C.J., and Coauthors (2013). Assessment of Global Cloud Datasets from Satellites:
689 Project and Database Initiated by the GEWEX Radiation Panel. Bull. Amer. Meteor. Soc., 94,
690 1031–1049, https://doi.org/10.1175/BAMS-D-12-00117.1.

van Diedenhoven, B., Cairns, B., Geogdzhayev, I.V., Fridlind, A.M., Ackerman, A.S., Yang, P., and Baum, B.A. (2012). Remote sensing of ice crystal asymmetry parameter using multi-directional polarization measurements – Part 1: Methodology and evaluation with simulated measurements, *Atmos. Meas. Tech.*, 5, 2361–2374, https://doi.org/10.5194/amt-5-2361-2012.

van Diedenhoven, B., Cairns, B., Fridlind, A.M., Ackerman, A.S., and Garrett, T.J. (2013). Remote sensing of ice crystal asymmetry parameter using multi-directional polarization measurements – Part 2: Application to the Research Scanning Polarimeter, *Atmos. Chem. Phys*., 13, 3185–3203, https://doi.org/10.5194/acp-13-3185-2013.

van Diedenhoven, B., Ackerman, A.S., Fridlind, A.M., Cairns, B., and Riedi, J. (2020). Global statistics of ice microphysical and optical properties at tops of optically thick ice clouds. *J. of Geophys. Res. Atmos*., 125, e2019JD031811. https://doi.org/10.1029/2019JD031811.

Vaughan, M.A., and Coauthors (2009). Fully automated detection of cloud and aerosol layers in the CALIPSO lidar measurements. *J. Atmos. Oceanic Technol*., 26, 2034–2050, https://doi.org/10.1175/2009JTECHA1228.1.

Voigt, A., Albern, N., Ceppi, P., Grise, K., Li, Y., and Medeiros, B. (2021). Clouds, radiation, and atmospheric circulation in the present-day climate and under climate change. *WIREs Clim Change*,12:e694, https://doi.org/10.1002/wcc.694.

Wall, C.J., Norris, J.R., Gasparini, B., Smith, W.L., Thieman, M.M., and Sourdeval, O. (2020). Observational Evidence that Radiative Heating Modifies the Life Cycle of Tropical Anvil Clouds. *J. Climate*, 33, 8621–8640, https://doi.org/10.1175/JCLI-D-20-0204.1.

Welton, E. J., Campbell, J.R., Spinhirne, J.D., and. Scott, V.S (2001). Global monitoring of clouds and aerosols using a network of micro-pulse lidar systems. *Proc. SPIE*, 4153, 151–158, https://doi.org/10.1117/12.417040.

Welton, E.J., and Campbell, J.R. (2002). Micropulse Lidar Signals: Uncertainty Analysis. *J. Atmos. Oceanic Technol.*, 19, 2089–2094, https://doi.org/10.1175/1520-0426(2002)019<2089:MLSUA>2.0.CO;2.

Welton, E.J., Stewart, S.A., Lewis, J.R., Belcher, L.R., Campbell, J.R., and Lolli, S. (2018). Status of the NASA Micro Pulse Lidar Network (MPLNET): Overview of the network and future plans,

new Version 3 data products, and the polarized MPL. EPJ Web of Conferences, 176, https://doi.org/10.1051/epjconf/201817609003.

Wielicki, B.A., Cess, R.D., King, M.D., Randall, D.A., and Harrison, E.F. (1995). Mission to Planet Earth: Role of Clouds and Radiation in Climate, *Bull. of the Amer. Meteo. Soc*., 76(11), 2125-2154.

Wielicki, B.A., B.R. Barkstrom, E.F. Harrison, R.B. Lee III, G.L. Smith, and J.E. Cooper (1996). Clouds and the Earth's Radiant Energy System (CERES): An Earth Observing System experiment. *Bull. Amer. Meteor. Soc.*, 77, 853–868, https://doi.org/10.1175/1520-0477(1996)077,0853:CATERE.2.0.CO;2.

Winker, D.M., Vaughan, M.A., Omar, A., Hu, Y., Powell, K.A., Liu, Z., Hunt, W.H., and Young, S.A., (2009). Overview of the CALIPSO mission and CALIOP data processing algorithms. *J. Atmos. Oceanic Technol.,* 26, 2310–2323, https://doi.org/10.1175/2009JTECHA1281.1.

Xu, G., Schnaiter, M., and Järvinen, E. (2022). Accurate retrieval of asymmetry parameter for large and complex ice crystals from in-situ polar nephelometer measurements. *J. of Geophys. Res. Atmos.*, 127, e2021JD036071. https://doi.org/10.1029/2021JD036071.

Yang, P., Liou, K.N., Wyser, K., and Mitchell, D. (2000). Parameterization of the scattering and absorption properties of individual ice crystals, *J. Geophys. Res*., 105, 4699-4718.

Yang, P., Wei, H., Huang, H.-L., Baum, B.A., Hu, Y.X., Kattawar, G.W., Mishchenko, M.I., and Fu, Q. (2005). Scattering and absorption property database for nonspherical ice particles in the near- through far-infrared spectral region, *Appl. Opt.,* 44, 5512-5523.

Yang, P., Bi, L., Baum, B.A., Liou, K.N., Kattawar, G.W., Mishchenko, M.I., and Cole, B. (2013). Spectrally consistent scattering, absorption, and polarization properties of atmospheric ice crystals at wavelengths from 0.2 mm to 100 mm. *J. Atmos. Sci*., 70, 330–347, https://doi.org/10.1175/JAS-D-12-039.1.

Yang, P., Hioki. S., Saito, M., Kuo, C.-P., Baum, B.A., Liou, K.-N. (2018). A reviw of ice cloud optical property models for satellite remote sensing, *Atmosphere* 2018, 9, 499; doi:10.3390/atmos9120499.

Yang, P., Ding, J., Panetta, R.L., Liou, K.-N., Kattawar, G.W., Mishchenko, M.I. (2019). On the convergence of numerical computations for both exact and approximate solutions for

749 electromagnetic scattering by nonspherical dielectric particles, *Progress In Electromagnetics*
750 *Research*, 164, 27-61.
751 Yi, B. (2022). Diverse cloud radiative effects and global surface temperature simulations induced
752 by different ice cloud optical property parameterizations. *Sci. Rep.,* **12**, 10539,
753 https://doi.org/10.1038/s41598-022-14608-w
754 Yorks, J., McGill, M., Hlavka, D., and Hart, W. (2011). Statistics of Cloud Optical Properties from
755 Airborne Lidar Measurements. *J. of Atmos. and Ocean. Tech*., 28 (7): 869-883
756 [10.1175/2011JTECHA1507.1].
757 Zelinka, M.D., Myers, T.A., McCoy, D.T., Po-Chedley, S., Caldwell, P.M., Ceppi, P., and Taylor, K.
758 E. (2020). Causes of Higher Climate Sensitivity in CMIP6 Models. Geophys. Res. Lett., 47(1),
759 e2019GL085782. https://doi.org/10.1029/2019GL085782.